Pumped heat energy storage with liquid media: Thermodynamic assessment by a Brayton-like model

D. Salomone-González[a], J. González-Ayala[b], A. Medina[b,c], J.M.M. Roco[b,c], P. L. Curto-Risso[a], A. Calvo Hernández[b,c]

[a]*Facultad de Ingeniería, Universidad de la República, Montevideo, Uruguay*
[b]*Instituto Universitario de Física Fundamental y Matemáticas (IUFFyM), Universidad de Salamanca, 37008 Salamanca, Spain*
[c]*Departamento de Física Aplicada, Universidad de Salamanca, 37008 Salamanca, Spain*

Abstract

A thermodynamic model for a steady state pumped heat energy storage in liquid media is presented: it comprises a coupled Brayton-like heat pump and heat engine cycles connected to a cryogenic liquid and a hot molten salt by counter-flow heat exchangers. The model considers non-isothermal heat transfers between the working fluid and the liquid media and explicitly includes a set of parameters accounting for the main internal and external losses, heat leak, and pinch point effects for both the heat pump (charge) and heat engine (discharge) modes. Specific expressions for the main magnitudes in the charge (as the input power and coefficient of performance) and discharge (as power output and efficiency) modes and the global round trip efficiency have been analytically derived in terms of isentropic efficiencies of the compressor and turbine, pressure losses in the heat exchange processes, effectivenesses of the external counter-flow heat exchangers, and coupling between the working fluid and the storage and cryogenic liquid media. Round trip efficiencies around of $35-40\%$ have been obtained, internal losses being those with main negative influence on the calculated values.The strong constraints imposed by the pinch point effects and liquid media have been analyzed. The model provides a thermodynamic assessment of the main involved processes and their interplay for a selected arrangement (molten salts, cryogenic fluid, and the charge and discharge power blocks) in order to check parametric strategies for thermodynamic optimisation and design. These strategies are based on a reduced set of parameters of the overall installation and without the high computational costs of dynamical models.

Keywords: Energy Storage, Molten Salts, Coupled Brayton Model, Round Trip Efficiency, Internal and External irreversibilities.

1. Introduction

Electrical energy storage (EES) is considered as a promising technology for large-scale implementation [1] as it could improve power supply stability [2] in the power grid avoiding variability [3]. A particular type of EES is the so-called pumped heat energy storage (PHES), which in a charging process stores heat from a cold reservoir in a hot reservoir using a heat pump (HP) cycle and then, during a discharge process, heat is converted in electricity by a heat-work conversion heat engine (HE) cycle. Its independence on geographical and geological conditions suffered by most conventional pumped hydro storage and compressed air energy storage systems, motivates a high research interest nowadays [4]. Most works are focused on material selection [5], short-term storage in hybrid and intermittent energy generation systems [6], and grid storage [7]. In PHES systems usually the working fluid is a single-phase gas operating a Brayton-like cycle [8] or an appropriate fluid operating a subcritical, transcritical or organic Rankine-like cycle [9]. Also research is emphasized on thermoeconomic design optimization [10] and integration of solar and eolic resources [11]. Most thermal energy storage (TES) media are based on sensible packed-bed materials due to its wide temperature range, high efficiency and small pressure losses [8]. This kind of TES has been studied for large scale electric applica-

tions [12], using thermodynamic analysis [13] with main internal and external losses [14], parametric optimization [15], and response to cycle duration perturbations [16]. A detailed comparison in packed-bed materials using both Joule-Brayton and Rankine-like cycles was recently performed by Dietrich using exergoeconomic analyses [17].

For liquid media storage, conceptual design for cycles was first performed by Morandin *et al*. [9] and later applied to molten salts and synthetic oil as sensible heat storage with air as working fluid [18]. Round trip efficiency (RTE) estimations around of 0.55 were reported assuming isentropic efficiencies of 0.9. Rankine-based cycles were applied to transcritical CO_2 working fluid and water as TES systems [10]. With above studies as reference, Fernandez *et al*. [11] proposed more complex arrangements focused on the integration in a single system of renewable sources operating at different temperature levels and oriented to applications at different scales (mid/high temperature solar power plants and smaller-scale renewable installations). In this analysis, clear advantages for exploitation of synergies at different power ranges were reported. In the same line, the possibility of solar-PHES systems employing technology developed by the concentrated solar power industry was analyzed by Farres *et al*. [19]. The need for arrangements with intercooled stages at the cold side of the cycle was pointed out. Very recently, Frate *et al*. [20] reported a multi-criteria

Nomenclature	
a	temperature ratio
c_p	specific heat capacity at constant pressure (J/kgK)
c_v	specific heat capacity at constant volume (J/kgK)
C	heat capacity (W/K)
k	dimensionless factor $\left(\frac{\gamma-1}{\gamma}\right)$
$\dot{m}$	mass flow (kg/s)
P	pressure (atm)
$\dot{Q}$	heat flow (W)
r	pressure ratio
T	temperature (K)
W	work (W)
Y	dimensionless factors
Z	dimensionless factors
Greek Letters	
γ	adiabatic coefficient
Γ	dimensionless factor
ϵ	efficiencies
η	efficiency of the heat engine
ν	COP of the heat pump
ξ	heat leak factor
ρ	dimensionless coefficients
Φ	round trip efficiency
Subscript	
c	compressor
H	high pressure
L	low pressure
t	turbine
w	working fluid
0	ambient
Acronyms	
CFD	computational fluid dynamic
COP	coefficient of performance
EES	electrical energy storage
HE	heat engine
HP	heat pump
$HTHP$	high temperature heat pump
$LMTD$	logarithmic mean temperature difference
NTU	number of transfer units
$PHES$	pumped heat energy storage
PP	pinch point
RTE	round trip efficiency
TES	thermal energy storage

optimization analysis of a Rankine cycle with low-grade thermal energy integration using trade-off figures of merit based in layouts with and without internal regeneration in the charge and discharge operation modes. They conclude that regeneration is effective, with better global performances as it relaxes the trade-off between the objectives. Also recently, Hassan *et al*. [21] reported a thermodynamic analysis of a high-temperature heat pump driving an organic Rankine cycle by means of an energy storage system. The work reports latent and sensible heat for different refrigerants and configurations in order to maximize the advantages of the refrigerant subcooling.

Unlike the solid media, the liquid storage offers two additional advantages: a) the pressure inside the tanks is independent of the pressure of the cyclic working fluid, allowing lower costs in the tanks and more compact compression and expansion devices with smaller pressure drops; and b) the temperature inside each tank remains almost constant, avoiding the problems associated to the propagation of the hot front in solid storage. On the contrry, as noted by Laughlin [7], the main drawback relies on the need of two tanks for each reservoir, in addition to some technical requirements which must be met in order to get an appropriate integration on the overall system. Concerning to suitability of liquid media and working fluids, many work has been reported. In particular, Zaversky et al. [22] analyzed a model for the transient molten salt two-tank thermal storage, Peger *et al*. [23] studied the nitrate salts for sensible and latent heat storage, and cost benefits for a selection of different salts was reported by Turchi *et al*. [24]. For the cryogenic liquids [25], lower melting temperatures and not too high boiling temperatures at low pressure are two valuable requirements to get a wide stable liquid phase at atmospheric or sub-atmospheric pressures, as noted by Davenne *et al*. [26]. In what regards to the working fluid, properties of noble gases and binary mixtures on Brayton applications have been reported by Tournier and El-Genk [27] and energy and exergy analysis were conducted by Habibi et al. [28]. Also, non-toxicity and no corrosion are required conditions. Thus, potential candidates are monoatomic noble gases (specially argon (Ar) since helium (He) is quite expensive) and diatomic gases as air and nitrogen (N_2), since hydrogen (H_2) is highly inflammable [7]. Between the two usual options, argon allows higher temperature and lower pressure levels and (almost) constant heat capacity, while N_2 allows the use of turbines and compressors well tested in conventional cyclic heat devices.

Methodologically, most of the models are based on computational fluid dynamic (CFD) simulations on the transient behavior [8], integration of solar energy [11] and/or commercial software through exergoeconomic analyses [17], and evaluation on thermal and mechanical performance of the hot tank [29]. Theoretical studies fully based on thermodynamic frameworks assuming Carnot-like models were conducted by Tess [30] and Chen et al. [31], while works based on weak-dissipative models were reported by Guo et al. for both pumped thermal [32] and cryogenic storage [33]. These authors also reported a recuperative Brayton-like arrangement model [34]. Optimized performance regimes were calculated.

A common characteristic of the above fully theoretical models is the assumption of constant temperature external sources. For liquid storage, this assumption is quite unrealistic as the liquid phase in the tanks changes temperature according to working fluid and heat exchanger requirements. To overcome this problem, the main goal of this paper is to formulate a novel Brayton-like arrangement for liquid storage using more realistic non-isothermal charge/discharge processes for a working fluid coupled to liquid TES by counter-flow heat exchangers, as the conceptual picture in Fig. 1 shows.
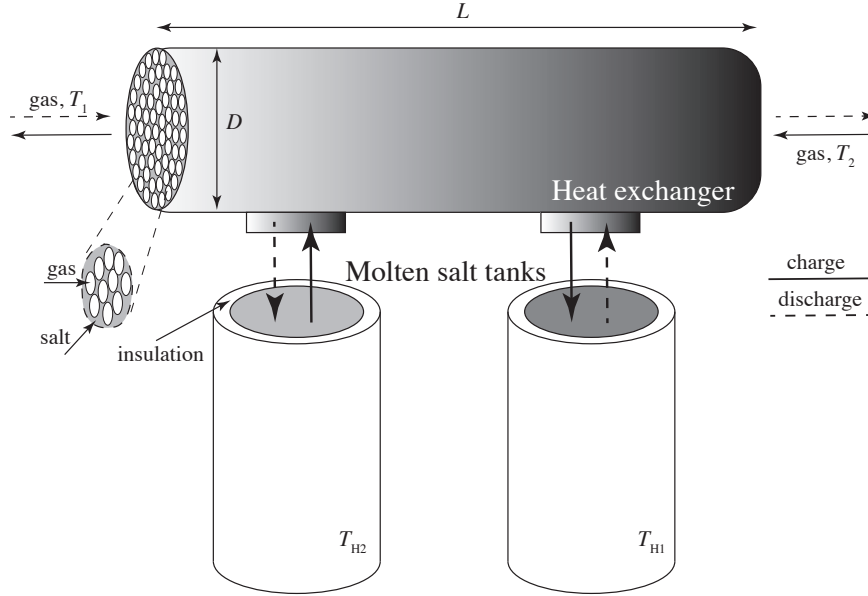
Figure 1: Sketch of the interaction between the counter-flow heat exchanger and the working fluid along the charge and discharge steps in the hot medium in order to illustrate the corresponding heat transfers.

The proposed model accounts for the description of both the charge and discharge modes and their interactions with the TES system, including internal losses for compressors and expander (turbine), pressure drops for the working fluid, heat leak to the environment, external coupling of the working fluid with TES materials, and pinch point effects. It allows explicit analytical and numerical results for the main involved magnitudes as efficiency and power output of the HE cycle, the coefficient of performance (COP) and the power input of the HP cycle, and the round trip efficiency of the overall device in terms of the considered losses. From this, an additional advantage of the model is its ability to check parametric strategies for optimization and design based on a reduced set of parameters accounting for the molten salts, the cryogenic storage fluid, and the charge and discharge power blocks. In brief, it constitutes a comprehensive thermodynamic description of the main processes and their interplay for a selected arrangement without the high computational costs of dynamical models.

The paper is structured as follows. Section 2 briefly compiles some thermal properties of usual molten salts and cryogenic liquids which will be used to obtain particular numerical results. Section 3 contains the description of the HE and HP cycles as well as their coupling for the whole thermodynamic model. Section 4 shows numerical results for the efficiency of the HE, COP of the HP and overall round trip efficiency, with special emphasis on the effect of internal and external losses, heat leak, and pinch points effects. Particular examples for some systems in Table 1 are also worked out in this section to show explicit $T - S$ behaviors for HE and HP cycles, as well as to calculate specific values of the corresponding efficiency, COP, and round trip efficiency. Finally, in Section 5, discussion of the main results, some perspectives, and a brief summary are presented.

2. Molten salts and cryogenics liquids

Some relevant physical properties of usual molten salts [24] and standard cryogenic liquids [26] in thermal storage are compiled in Tables 1 and 2, respectively. For completeness, costs are also shown. These tables include the specific heat capacity c_p, density ρ, and volumetric heat capacity ρc_p, relative to the value for solar salt. The magnitude ρc_p is a key factor in determining the volume of the storage liquid tanks, because of the tank size is inversely proportional to $\rho c_p \Delta T$. Note in Table 1 that the only molten salts with a larger volumetric heat capacity than solar salt (NaNO$_3$/KNO$_3$) are sodium nitrate (NaNO$_3$) and the ternary potassium/sodium/lithium carbonate blend (K$_2$CO$_3$/Na$_2$CO$_3$/Li$_2$CO$_3$). Solar salt shows a thermal decomposition temperature about 850 K, which progressively increases from pure sodium nitrate and potassium nitrate (KNO$_3$) to binary potassium/magnesium chloride blend (KCl/MgCl$_2$) and then for ternary combinations. For the cryogenic liquids, the liquid phase stability determined by the boiling point range is around 376 K for the euthetic salt and around 350 K for anhydrous methanol, n-hexane, and anhydrous methanol. A smaller value of 230 K is presented by the n-propane. These T_{min} (solidification temperature) and T_{max} values are very relevant as they rule the extreme temperatures of the working fluid and, as consequence, the pressure ratios of the compressor and expander.

3. Thermodynamic model

The proposed overall arrangement consists in a combination of a Brayton-like HP cycle followed by a Brayton-like HE cycle. Fig. 2a depicts the T-S diagram for the charge HP-cycle and Fig. 2b a scheme of the corresponding components showing the interaction of the compressor and expander with the cryogenic

3

Salt	T_{min} (K)	T_{max} (K)	c_p (kJ/kgK)	ρ (kg/l)	ρc_{prel}	Price (USD/kg)
Solar	511	858	1.55	1.71	1.00	0.80
$NaNO_3$	579	793	1.62	1.82	1.11	0.68
KNO_3	607	873	1.40	1.78	0.94	1.00
$KCl/MgCl_2$	699	> 1070	1.03	1.94	0.75	0.35
$MgCl_2/NaCl/KCl$	658	> 1070	1.14	1.93	0.83	0.22
$ZnCl_2/NaCl/KCl$	473	> 1070	0.92	2.08	0.72	0.80
$K_2CO_3/Na_2CO_3/$ $/Li_2CO_3$	671	1073	1.79	2.01	1.36	2.50

Table 1: Some thermal properties and costs of solar salt and alternative salts for the high temperature storage, adapted from Turchi [24]. T_{min} represents the melting point or approximate liquidus point for non-eutectic salts. T_{max} the thermal stability temperature. Heat capacity c_p, density ρ, and volumetric heat capacity, ρc_{prel}. All these properties are assumed as constant.

Cryogenic Fluid	T_{min} (K)	T_{max} (K)	c_p (kJ/kgK)	ρ (kg/l)	Price (USD/kg)
Anhydrous Ethanol	158.8	351.2	2.46	0.783	0.43 [35]
N-Hexane	177.9	342.0	1.65	0.655	0.70 [7]
Anhydrous Methanol	175.3	337.5	2.55	0.787	0.30 [19]
N-Propane	85.3	230.9	2.25	0.581	0.24 [35]
Euthetic Salt (20% NaCl)	255.6	376.9	3.11	1.15	0.50 [19]

Table 2: Some thermal properties for the indicated cryogenic liquid storage. T_{min} denotes the melting point, T_{max} is the boiling temperature, c_p the specific heat capacity, and ρ the density (all of them assumed as constant) [25].

liquid and the storage reservoir. In Fig. 3 the same is done for the discharge HE mode. A simplified $T-S$ picture of the whole PHES system is shown in Fig. 4. In both operation modes, the liquid media is stored in four tanks at different constrained temperatures, in such a way that adequate integration profiles for the charge/discharge processes holds by counter-flow heat exchangers. A brief description of the whole thermodynamic model is the following:

- *Charge; Fig. 2*: The working fluid enters in the HP compressor at state 3 and after a non-isentropic compression (step 3 → 2) gets its maximum pressure and maximum temperature. Then, heat rejection by the working fluid with a pressure drop $\Delta P_H = P_2 - P_1$ is used in the counter-flow heat exchanger to increase the temperature of the molten salt from T_{H2} to T_{H1} as the working fluid is cooled down along process 2 → 1. Next, the working fluid expands in a non-isentropic process 1 → 4 getting its lowest temperature and pressure. In the next step, the working fluid is slowly heated up by the heat flow coming from the cold liquid material initially at temperature T_{L2}; then, the cold storage liquid diminishes its temperature to T_{L1} while the working fluid increases its temperature along step 4 → 3 with a pressure drop $\Delta P_L = P_4 - P_3$, recovering the initial state at temperature T_3 and pressure P_3.

- *Discharge; Fig. 3*: The working fluid undergoes a non-isentropic compression 4 → 1; then it is heated with a pressure drop $\Delta P_H = P_1 - P_2$, across the temperature gap T_1-T_2 by the heat delivery in the counter-flow heat exchanger of the hot storage molten salt, which in turn decreases its temperature from T_{H1} to T_{H2}. Afterwards, the hot working fluid at T_2 is expanded in the non-isentropic

turbine (2 → 3), and finally, it is cooled to its initial temperature T_4 experiencing a pressure drop $\Delta P_L = P_3 - P_4$. The heat delivered in this step by the working fluid allows the increase of temperature of the cold liquid medium from T_{L1} to T_{L2} by means of the (cold) counter-flow heat exchanger.

As detailed above, the model incorporates internal irreversibilities coming from non-isentropic expansion and compression processes in the turbine (expander) and compressor, respectively, and from pressure drops in the heater and in the cooler processes. The model also takes into account pinch point (PP) effects (see Fig. 4 and Sec. 4.4) and heat leaked to the environment coming from the hot molten salt (not shown in Figs. 2 and 3; see later for a mathematical description) while heat leak from the liquid cold storage is assumed to be negligible, which is a reasonable assumption at least for short operation times. After the end of HE cycle and in order to recuperate the initial conditions of the HP cycle, a heat exchanger could be necessary for process $T_{3HE} \rightarrow T_{3HP}$. This feature is out of the scope of this work because it is only considered steady state performance and transient behaviours are avoided.

3.1. Thermodynamic analysis: Heat pump cycle

The HP cycle (charging mode) with the working fluid running in an anti-clockwise direction is first considered. All specified states thus refer to Fig. 2. Pressure drops of the fluid along the hot and cold sides (ΔP_H and ΔP_L, respectively) are accounted by the coefficients ρ_H and ρ_L, given by [36]:

$$\rho_H = \left(\frac{P_1}{P_2}\right)^k = \left(\frac{P_2 - \Delta P_H}{P_2}\right)^k, \qquad (1)$$

$$\rho_L = \left(\frac{P_3}{P_4}\right)^k = \left(\frac{P_4 - \Delta P_L}{P_4}\right)^k, \qquad (2)$$

where $k = \frac{\gamma-1}{\gamma}$ and $\gamma = c_p/c_V$ is the adiabatic coefficient of the working fluid. It is common to account for internal losses at the compressor and turbine using isentropic efficiencies for the compression and expansion processes, ϵ_c and ϵ_t, respectively, given by [37]:

$$\epsilon_c = \frac{T_{2s} - T_3}{T_2 - T_3}, \qquad (3)$$

$$\epsilon_t = \frac{T_1 - T_4}{T_1 - T_{4s}}, \qquad (4)$$

where T_{2s} and T_{4s} refer to isentropic processes. The variables a_c and a_t are defined in terms of the compression ratios, $r_c \equiv P_2/P_3$ for the the compressor and $r_t \equiv P_1/P_4$ for the expander (turbine). They are given as:

$$a_c = \frac{T_{2s}}{T_3} = r_c^k = \left(\frac{P_2}{P_3}\right)^k = \left(\frac{P_2}{P_4 - \Delta P_L}\right)^k, \qquad (5)$$

$$a_t = \frac{T_1}{T_{4s}} = r_t^k = \left(\frac{P_1}{P_4}\right)^k = \left(\frac{P_2 - \Delta P_H}{P_4}\right)^k. \qquad (6)$$

According to Eqs. (1) and (2), a_t and a_c are linked by the relation

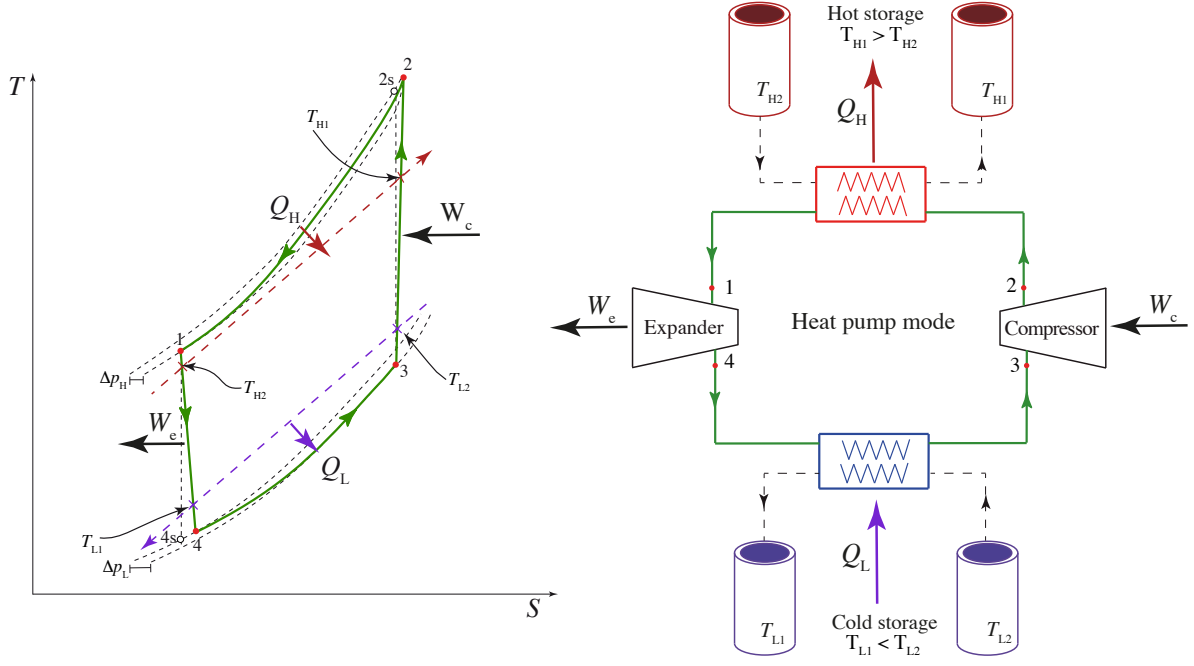$$a_t = \rho_H \rho_L a_c. \qquad (7)$$

Figure 2: a) $T - S$ diagram of the charge HP cycle and in b) scheme of the corresponding components.
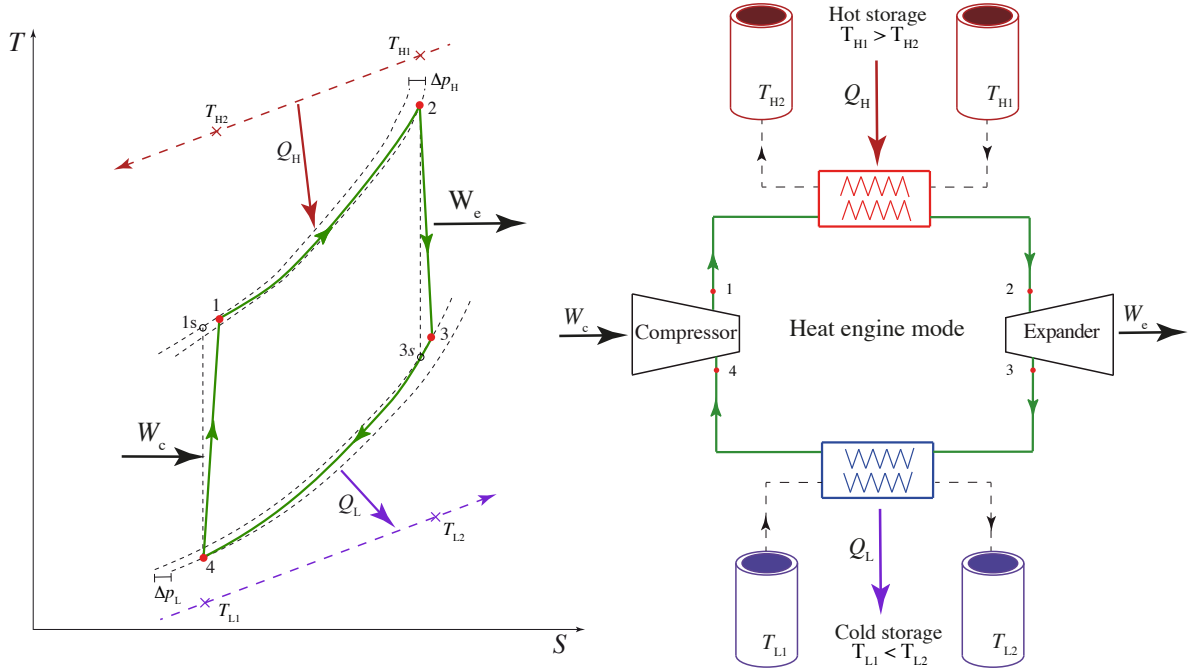

Figure 3: a) $T - S$ diagram of the discharge HE cycle and in b) scheme of the corresponding components.

The input power on the working fluid by the compressor W_c and the power output W_t in the expander (turbine) are:

$$W_c = C_w(T_2 - T_3) = C_w T_3 \left(\frac{a_c - (1 - \epsilon_c)}{\epsilon_c} \right), \qquad (8)$$

and

$$W_t = C_w(T_1 - T_4) = C_w T_1 \epsilon_t \left(\frac{a_t - 1}{a_t} \right), \qquad (9)$$

where $C_w(\equiv \dot{m}_w c_{pw})$ is the per-unit-time heat capacity of the working fluid.

The irreversible heat transfers between the working fluid and the external liquid storages take place along temperature dependent processes as the heat capacities remain finite. Then, the liquid materials change temperature along the counter-flow exchangers with the working fluid. The temperatures of the working fluid along $2 \rightarrow 1$ should be greater than the high-temperature thermal energy storage system (the molten salts) at

5

T_{H1}, so that an amount of heat, $\dot{Q}_H$, is absorbed by the salt reservoir which increase its temperature from T_{H2} to T_{H1}. Opposite, the temperatures of the working fluid along $4 \rightarrow 3$ should be smaller than the low-temperature thermal energy storage, so that an amount of heat, $\dot{Q}_L$, is delivered as the temperature decreases from T_{L2} to T_{L1}.

The corresponding heat transfers can be properly taken into account by using the logarithmic mean temperature difference (LMTD) [38] between the hot and cold feeds at each end of the counterflow exchanger or by using the Number of Transfer Units (NTU) method [39]. Here, and in order to avoid very specific technical details, it is assumed an usual treatment of finite time thermodynamics in which the heat rate of the working fluid $C_w(T_2 - T_1)$ and the heat rate in the hot side of the counterflow heat exchangers $C_H(T_{H1} - T_{H2})$ are balanced through a global effectivenesses ϵ_H. In the same way the heat rate of the working fluid $C_w(T_3 - T_4)$ and the heat rate in the cold side of the counterflow heat exchangers $C_L(T_{L2} - T_{L1})$ are balanced through a global effectivenesses ϵ_L [38]. Then $\dot{Q}_H$ and $\dot{Q}_L$ can be written as:

$$\dot{Q}_H = C_w(T_2 - T_1) = C_H(T_{H1} - T_{H2}) = C_{H,min}\epsilon_H(T_2 - T_{H2}), \quad (10)$$

and

$$\dot{Q}_L = C_w(T_3 - T_4) = C_L(T_{L2} - T_{L1}) = C_{L,min}\epsilon_L(T_{L2} - T_4), \quad (11)$$

where C_w is the heat capacity of the working fluid and $C_{H,min} = min(C_H, C_w)$ and $C_{L,min} = min(C_L, C_w)$ are the minimal heat capacities of the the hot and cold TES media, respectively.

By combining the above equations it is obtained that:

$$T_{H1} = T_{H2} + \Gamma_H(T_2 - T_1) \quad (12)$$

and

$$T_{L1} = T_{L2} - \Gamma_L(T_3 - T_4), \quad (13)$$

where $\Gamma_H = \frac{C_w}{C_H}$ and $\Gamma_L = \frac{C_w}{C_L}$. These equations play an important role as they link the salt temperatures of the hot tanks (T_{H1} and T_{H2}) an of the cryogenic liquid (T_{L1} and T_{L2}) with the temperatures of the working fluid in the extreme states of the HP cycle in terms of dimensionless coefficients Γ_H and Γ_L.

The outlet temperatures in the compressor, T_2, and expander, T_4, can be worked out in terms of the isentropic efficiencies (ϵ_c and ϵ_t), pressure losses (ρ_H and ρ_L), and effectivenesses (ϵ_H and ϵ_L). By using Eqs. (3), (4), (7), (12) and (13), T_1, T_2, T_3, T_4 and also T_{H1} and T_{L1} can be expressed in terms of T_{H2} and T_{L2}. The reason for selecting these temperatures is due to practical purposes: T_{L2} is the starting temperature of the cryogenic fluid in the charging process and can be fixed to a certain value, for example, the environment temperature, and T_{H2} is the temperature in the salt tank (obviously, greater than the melting point of the salt) at the beginning of the charge cycle. The relevant

temperatures of the HP cycle are given by:

$$T_1 = \frac{T_{H2}\epsilon_H + T_{L2}Z_1\epsilon_L(1 - \epsilon_H)}{1 - Z_1Z_2(1 - \epsilon_H)(1 - \epsilon_L)}, \quad (14)$$

$$T_3 = \frac{T_{L2}\epsilon_L + T_{H2}Z_2\epsilon_H(1 - \epsilon_L)}{1 - Z_1Z_2(1 - \epsilon_H)(1 - \epsilon_L)}, \quad (15)$$

$$T_2 = T_3Z_1, \quad (16)$$

$$T_4 = T_1Z_2, \quad (17)$$

with $a_t = \rho_H\rho_L a_c$, as mentioned before, and

$$Z_1 \equiv \frac{a_c - (1 - \epsilon_c)}{\epsilon_c}, \qquad Z_2 \equiv \frac{a_t(1 - \epsilon_t) + \epsilon_t}{a_t}. \quad (18)$$

The COP of the HP cycle, $\nu \equiv \dot{Q}_H/(\dot{Q}_H - \dot{Q}_L)$, is given by:

$$\nu = \frac{Z_2\left(\frac{1-\epsilon_L}{\epsilon_L}\right) - \frac{1}{Z_1\epsilon_L} + \frac{T_{L2}}{T_{H2}}}{Z_2\left(\frac{1-\epsilon_L}{\epsilon_L} + \frac{T_{L2}}{T_{H2}}\frac{1-\epsilon_H}{\epsilon_H}\right) + \frac{Z_2}{Z_1} - \frac{1}{Z_1}\left(\frac{1}{\epsilon_H} + \frac{1}{\epsilon_L}\right) + \frac{T_{L2}}{T_{H2}}}. \quad (19)$$

Another irreversibility source is the unavoidable heat leak between the hot and cold sides of the overall plant. A detailed analysis of this point should include separately the charge and discharge modes, the interactions of the working fluid with the liquid media, the cycle time and, most important, the materials, sizing, and geometry of the salts tanks. Such analysis is out of the scope of this work. Here, it will be assumed only a heat leak between the molten salt sources T_{H1} and T_{H2} with the environment at temperature T_0, and a negligible heat leak due to the cold liquid storage. In the finite-time-thermodynamics framework an easy way to take into account this effect is by assuming an averaged, linear decreasing of the temperatures T_{H1} y T_{H2} with an effective proportionality factor ξ, so that the initial temperatures T_{H1} y T_{H2} decreases due to heat leak as:

$$\Delta T_{H1} = -\xi(T_{H1} - T_0), \quad (20)$$

$$\Delta T_{H2} = -\xi(T_{H2} - T_0). \quad (21)$$

This linear assumption has been corroborated by empirical results in the analysis of heat losses in two-tank thermal storage systems for concentrated solar power plants [40].

3.2. Thermodynamic analysis: Heat engine cycle

For the HE case all subscripts and processes refer to Fig. 3. The pressure drops of the working fluid in the hot (low) sides, ρ_H (ρ_L), are defined as:

$$\rho_H = \left(\frac{P_2}{P_1}\right)^k = \left(\frac{P_1 - \Delta P_H}{P_1}\right)^k, \quad (22)$$

$$\rho_L = \left(\frac{P_4}{P_3}\right)^k = \left(\frac{P_3 - \Delta P_L}{P_3}\right)^k. \quad (23)$$

The internal losses for the compressor and turbine processes are quantified through the corresponding isentropic efficiencies, ϵ_c and ϵ_t, respectively:

$$\epsilon_c = \frac{T_{1s} - T_4}{T_1 - T_4}, \quad (24)$$

$$\epsilon_t = \frac{T_2 - T_3}{T_2 - T_{3s}}. \quad (25)$$

The isentropic pressure ratios for the turbine, r_t, and compressor, r_c, are given now by the relations $r_c \equiv P_1/P_4$ and $r_t \equiv P_3/P_2$ and the corresponding a_c and a_t are now

$$a_c = \frac{T_{1s}}{T_4} = r_c^k = \left(\frac{P_1}{P_4}\right)^k = \left(\frac{P_1}{P_3 - \Delta P_L}\right)^k, \tag{26}$$

$$a_t = \frac{T_2}{T_{3s}} = r_t^k = \left(\frac{P_2}{P_3}\right)^k = \left(\frac{P_1 - \Delta P_H}{P_3}\right)^k, \tag{27}$$

which are linked by the same relation than in the HP cycle

$$a_t = \rho_H \rho_L a_c. \tag{28}$$

In the HE mode the high temperature liquid store decreases its temperature from T_{H1} to T_{H2} as the working fluid temperature increases from T_1 to T_2 while absorbing heat through the heat exchanger. Opposite to this, the low temperature store increases its temperature from T_{L1} to T_{L2} as the working fluid temperature decreases from T_3 to T_4 while delivering heat through the heat exchanger. As for the HP-cycle, these heat transfers can be written in terms of the effectivenesses as:

$$\dot{Q}_H = C_w(T_2 - T_1) = C_H(T_{H1} - T_{H2}) = C_{H,min}\epsilon_H(T_{H1} - T_1), \tag{29}$$

and

$$\dot{Q}_L = C_w(T_3 - T_4) = C_L(T_{L2} - T_{L1}) = C_{L,min}\epsilon_L(T_3 - T_{L1}), \tag{30}$$

which link the temperatures of the hot tanks (T_{H1} and T_{H2}) and the cryogenic liquid (T_{L1} and T_{L2}) with the temperatures of the working fluid in the extreme states of the HE cycle. From the above equations, the temperatures of the salt tanks (T_{H2}, T_{H1}) and of the cryogenic liquid (T_{L2} and T_{L1}) in terms of the corresponding dimensionless coefficients Γ_H and Γ_L are given as:

$$T_{H2} = T_{H1} - \Gamma_H(T_2 - T_1), \tag{31}$$

and

$$T_{L2} = T_{L1} + \Gamma_L(T_3 - T_4), \tag{32}$$

with $\Gamma_H = \frac{C_w}{C_H}$ and $\Gamma_L = \frac{C_w}{C_L}$. As for the HP mode, in the above equations C_w is the heat capacity of the working fluid and $C_{H,min}$ and $C_{L,min}$ are the minimal heat capacities of the the hot and cold TES media, respectively.

By using Eqs. (24), (25), and (28), T_1, T_2, T_3, T_4, T_{H2} and T_{L2} can be expressed in terms of T_{H1} and T_{L1}. The explicit expressions are given by

$$T_2 = \frac{T_{H1}\epsilon_H + T_{L1}Y_1\epsilon_L(1 - \epsilon_H)}{1 - Y_1Y_2(1 - \epsilon_H)(1 - \epsilon_L)}, \tag{33}$$

$$T_4 = \frac{T_{L1}\epsilon_L + T_{H1}Y_2\epsilon_H(1 - \epsilon_L)}{1 - Y_1Y_2(1 - \epsilon_H)(1 - \epsilon_L)}, \tag{34}$$

$$T_1 = T_4Y_1, \tag{35}$$

$$T_3 = T_2Y_2, \tag{36}$$

where

$$Y_1 \equiv \frac{a_c - (1 - \epsilon_c)}{\epsilon_c}, \qquad Y_2 \equiv \frac{a_t(1 - \epsilon_t) + \epsilon_t}{a_t}, \tag{37}$$

and $a_t = a_c\rho_H\rho_L$. From the above equations, the efficiency of the Brayton heat engine in the discharge phase, $\eta = \dot{W}_{out}/\dot{Q}_H = (\dot{Q}_H - \dot{Q}_L)/\dot{Q}_H$, is given as:

$$\eta = 1 + \frac{T_{L1}\epsilon_L(Y_1Y_2(1 - \epsilon_H) - 1) + T_{H1}Y_2\epsilon_H\epsilon_L}{T_{H1}\epsilon_H(Y_1Y_2(1 - \epsilon_L) - 1) + T_{L1}Y_1\epsilon_H\epsilon_L}. \tag{38}$$

For the heat leak, the treatment is as for the HP cycle. Thus, only the heat leak between the molten salt source and the ambient with temperature T_0 will be considered assuming a negligible heat leak due to the coupling of the cold liquid storage. As a consequence, a linear decreasing of the temperatures T_{H1} y T_{H2} with a proportionality factor ξ is considered:

$$\Delta T_{H1} = -\xi(T_{H1} - T_0), \tag{39}$$

$$\Delta T_{H2} = -\xi(T_{H2} - T_0). \tag{40}$$

3.3. Overall performance

A sketch of the T-S diagram of both HP and HE cycles is depicted in Fig. 4 . Notice that there is a difference in temperature between the starting point of the HP (label 3HP) and the ending point of the HE cycle (label 4HE). This should be considered in order to couple both cycles since a decrease in temperature is needed to pass from charge to discharge. The overall performance of the PHES system is defined in terms of the steady-state round trip efficiency [8], Φ, as the ratio between power generated in the heat engine $\dot{W}_{out}^{HE}$ and power input in the heat pump $\dot{W}_{net}^{HP}$. Considering both magnitudes as positive Φ is given as:

$$\Phi = \frac{net\ power\ output}{net\ power\ input} = \frac{\dot{W}_{out}^{HE}}{\dot{W}_{net}^{HP}} = \frac{\eta\ \dot{Q}_H^{HE}}{v^{-1}\dot{Q}_H^{HP}} \tag{41}$$

where the last equality follows from the usual definitions of the efficiency $\eta = \dot{W}_{net}^{HP}/\dot{Q}_H^{HE}$ in terms of the heat rate absorbed by the heat engine and of the COP, $v = \dot{Q}_H^{HP}/\dot{W}_{net}^{HP}$, in terms of the heat rate exchanged in the condenser in the heat pump operation.

4. Results

From the model in the previous section, it is evident that any particular configuration performance needs the specification of a set of variables and parameter for both the HE and HP cycles as well as the constraints imposed by the liquid media. These points are considered below. Next, a general overview is done on the basis of each type of irreverversibility, and finally, some concrete results are given for some molten salts and cryogenics liquids in Tables 1 and 2.

4.1. Parameters and constraints

The compression ratios, r_c^{HE} and r_c^{HP}, are the fundamental independent variables. But also the model incorporates a set of parameter accounting for: a) internal irreversibilities (the isentropic efficiencies of the compressor and turbine (ϵ_c, ϵ_t) and the pressure drops in the high and low temperature sides (ρ_H, ρ_L));
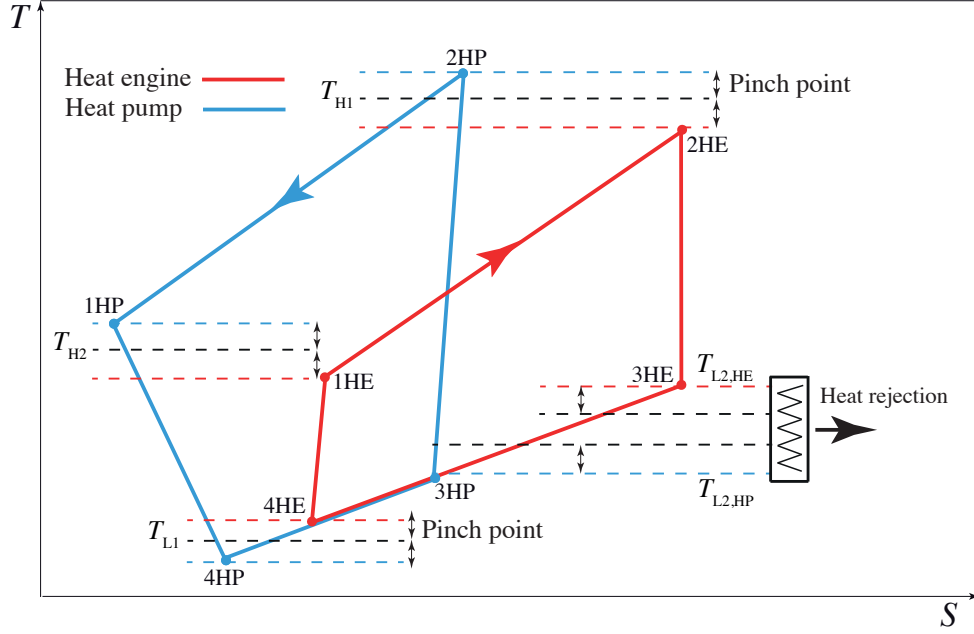
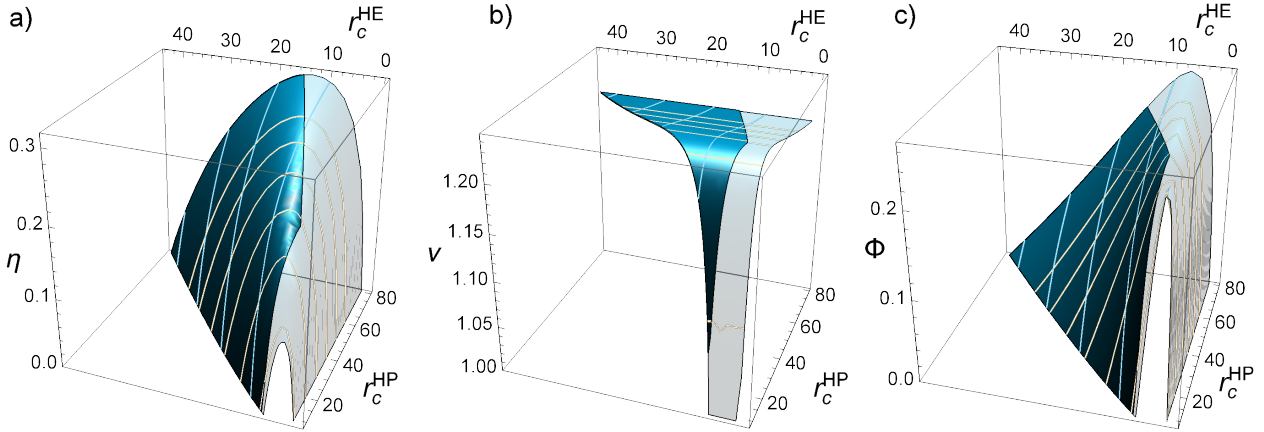Figure 4: $T - S$ setup of the whole thermodynamic cycle for the PHES system.

Figure 5: Behaviors of η, ν and Φ in terms of the compression ratios r_c^{HE} and r_c^{HP}. Baseline arrangement: $\epsilon_c = \epsilon_t = 0.9$, $\epsilon_H = \epsilon_L = 0.90$, $\Delta P = 0.02$, $\xi = 0.02$, $T_{H2}^{HP} = 500\,K$, $T_{L2}^{HP} = T_0 = 300\,K$, $T_{L1}^{HE} = 250\,K$, $\gamma = 1.4$, $\Gamma_H^{HE} = 1$, $\Gamma_L^{HE} = 0.4$, $\Gamma_H^{HP} = 0.9$, $\Gamma_L^{HE} = 1$, $PP_H = PP_L = 0\,K$. The transparent surfaces contains values without any constraint on the input parameters.

b) external irreversibilities by means of one additional parameter for the heat leak in the hot tanks (ξ) and two parameters for the coupling of the working fluid to the relevant external thermal energy storage (ϵ_H, ϵ_L); and c) one more parameter describing the nature of the working fluid (γ).

Concerning with the TES liquid media temperatures, some restrictions should be taken into account to keep the liquid nature of the salt and of the cryogenic medium. These features impose some corresponding bounds in the values of T_{H1}, T_{H2}, T_{L1}, and T_{L2}. So, according with values in tables 1 and 2, it is considered here that: a) in average the maximum temperature of the salt medium is $T_{max,salt} = 1200\,K \geq T_{H1}^{HP} = T_{H1}^{HE}$; b) in average the minimum temperature of the salt medium is $T_{min,salt} = 480\,K \leq T_{H2}$; c) in average the maximum temperature of the cryogenic liquid is $T_{max,cry} = 350\,K \geq T_{L2}$; and d) in

average the minimum temperature of the cryogenic medium is $T_{min,cry} = 85\,K \leq T_{L1}$.

Another key influence is played by the heat capacities which balance the heat transfers between the working fluid and the TES liquid media, as shown in Eqs. (12) and (13) for the HP-cycle and Eqs. (31) and (32) for the HE-cycle. Accordingly, dimensionless coefficients $\Gamma_H^{HE} = C_w/C_H \leq 1$, $\Gamma_L^{HE} = C_w/C_L \leq 1$ for the discharging mode and $\Gamma_H^{HP} = C_w/C_H \leq 1$, $\Gamma_L^{HP} = C_w/C_L \leq 1$ for the charging cycle are assumed. This assumption may require the fitting of the mass flow rate of the liquids according to $\Gamma = C_w/C_{H,L} = (\dot{m}c_p)_w/(\dot{m}c_p)_{H,L} \leq 1$.

The pinch point (PP) effects, minimum temperature difference between hot and cold streams within heat exchanger in the heat transfer process can be assumed as a compromise between rate and efficiency of the heat exchange and plays an important
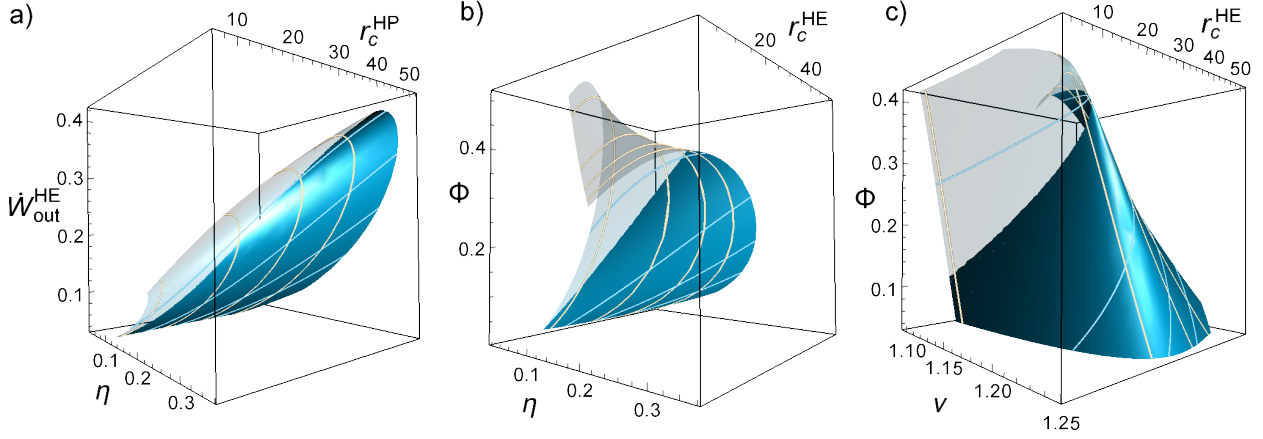
8

Figure 6: Behaviors of power output $\dot{W}_{out}^{HE}$ versus η, Φ versus η and Φ versus ν in terms of the compression ratios r_c^{HE} by the parametric elimination of r_c^{HP}. The baseline arrangement is as in previous figure.

role in the heat transfer process in the counter flow heat exchangers. Here, the PP-effects at the ends of the heat exchangers will be considered as a further approach to real systems [41].

4.2. General overview

The theoretical model in the last section has been implemented in Mathematica programming language, and the numerical results are presented below. For the sake of simplicity it is assumed that the parameters of the same nature have the same value in both charge and discharge cycles: $\epsilon_c^{HP} = \epsilon_c^{HE}$, $\epsilon_t^{HP} = \epsilon_t^{HE}$, $\epsilon_H^{HP} = \epsilon_H^{HE}$, $\epsilon_L^{HP} = \epsilon_L^{HE}$, $\Delta P_H^{HP} = \Delta P_L^{HP} = \Delta P_H^{HE} = \Delta P_L^{HE} = \Delta P$. As reference values in the baseline arrangement, and in agreement with usual reported values for these HE [36] and HP [38] cycles and optimization analysis [42], the following values of parameters are assumed: $\epsilon_c = \epsilon_t = 0.9$, $\epsilon_H = \epsilon_L = 0.90$, $\Delta P = 0.02 P_i$, where P_i is the pressure at the beginning of each process, and $\xi = 0.02$. All calculations below are presented in terms of the compression ratio of the HE-cycle, r_c^{HE} and of the HE-cycle, r_c^{HP} with input values of $T_{H2}^{HP} = 500$ K, $T_{L2}^{HP} = T_0 = 300$ K, $T_{L1}^{HE} = 250$ K, and $P_4 = 1$ atm. for an ideal diatomic gas as working fluid $\gamma = 1.4$.

Figure 5 shows the behavior of efficiency, η, coefficient of performance, ν, and round trip efficiency, Φ, in terms of compression ratios r_c^{HE}, r_c^{HP} and for the specified parameter values. The transparent surfaces correspond to unsuitable values according to constraints in the temperatures of the liquid media and pinch point effects. Probably the most important point to be noted is that there are noticeable limitations in the r_c^{HE} and r_c^{HP} values, so that lower r_c-values for the HE-cycle and, specially for the HP-cycle, are not suitable according to the imposed constraints. Also note the non-trivial behaviors of the efficiency in the HE cycle and of the COP in the HP cycle: roughly speaking, it is noted as in the charging mode (see Fig. 5b) the highest COP values are restricted for high r_c^{HE} and r_c^{HP} values while in the discharge model high efficiency values are obtained for smaller r_c^{HE} values. Altogether makes that the resulting round trip efficiency, Φ, inside the allowed r_c range, shows a non-trivial behavior but getting maximum values at moderate r_c^{HE} values (see Fig. 5c).

The above results and trends can be seen in a complementary way by the parametric elimination of the r_c^{HP} variable. These results are shown in Fig. 6 for the power output $\dot{W}_{out}^{HE}$ versus efficiency η of the HE-cycle (Fig. 6a), for the round trip efficiency Φ versus η (Fig. 6b), and for Φ versus ν (Fig. 6c). It is specially important to note the strong constraints experienced by the parameters (solid colours) at high compression ratios when faced with those without any restrictions (transparent surfaces).This provokes the disappearance of well-known behaviors when the HE cycle or the HP cycle work alone. For instance, the typical loop-like plots of the power output versus the efficiency in a HE cycle are only visible here in a small range of r_c^{HP} values (see Fig. 6a).

4.3. Internal and external irreversibility effects

The general configuration in Fig. 5 and Fig. 6 are amenable for discussing in detail the influence of irreversibility sources, both those affecting the internal (ϵ_c, ϵ_t, ρ_H, ρ_L) and external losses (ϵ_H, ϵ_L, ξ) as well as the PP effects. Instead of presenting particular results for each irreversibility parameter, a generic and global overview for each kind of irreversibility is shown. So, Fig. 7 displays the effects of the internal irreversibilities and Fig. 8 shows the effects of the external irreversibilities. From these figures, the following main general results can be pointed out:

a) As the irreversibilities increase (in the order green, blue, and red in Fig. 7 and Fig. 8), the physical arrangements are strongly restricted due to the progressively small range of values for the compression ratios of the HE and HP. This feature provokes the progressive disappearance of the well-known loop-like behaviors for η versus r_c^{HE} and ν versus r_c^{HP}, clearly visible in the most reversible configurations (green colours). Thus, the round trip efficiency values are smaller (below 0.4 in all cases) and only for very particular values of the HP and HE compression ratios.

b) When comparing the effects of the internal (Fig. 7) and external (Fig. 8) losses, the above trends are the same but, in the case of internal irreversibilities the effects are much greater (note the different vertical scales of these figures).
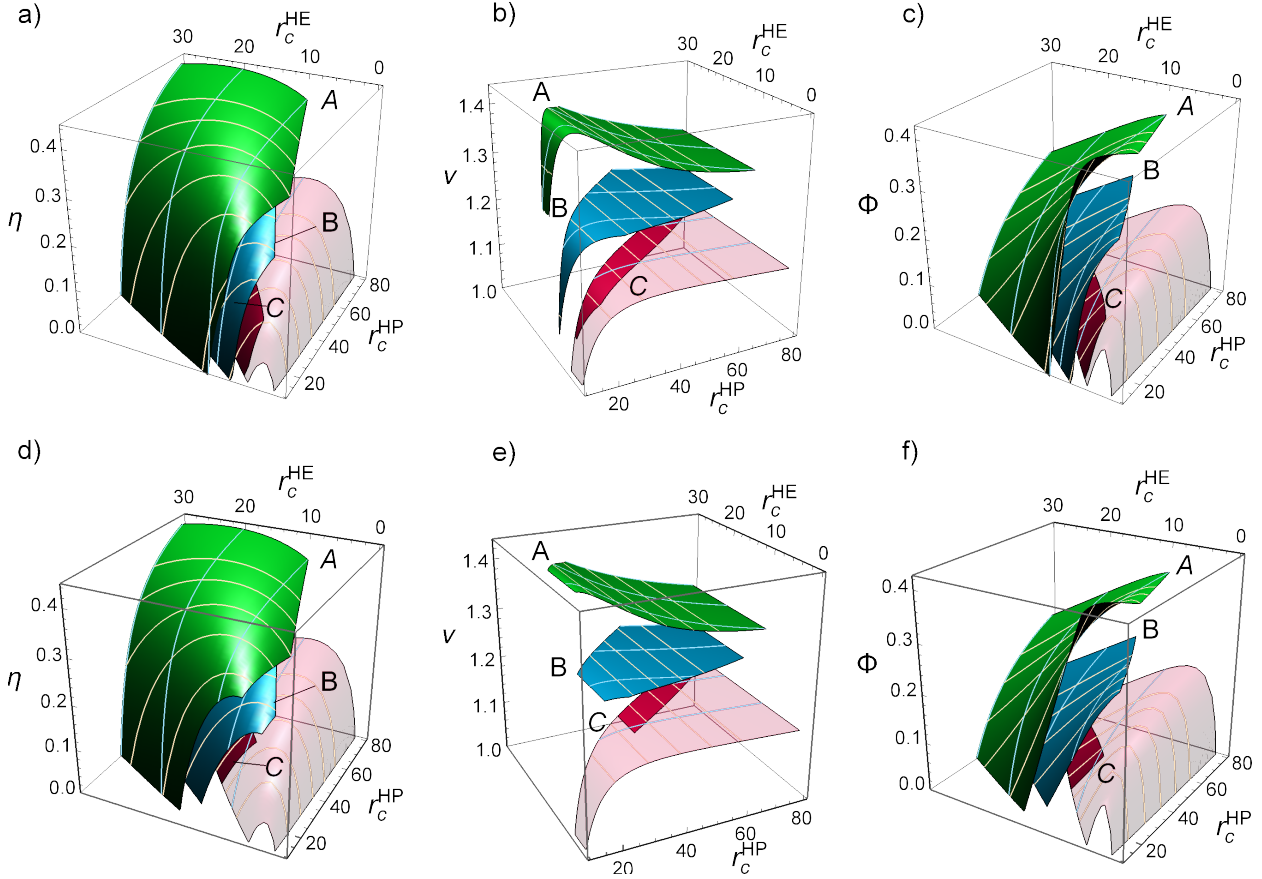
Figure 7: In (a)-(c): Effects of the internal irreversibilities on the physically acceptable values of η, ν, and Φ versus r_c^{HE} and r_c^{HP} without PP ($PP_H = PP_L = 0$). In (d)-(f) the same but with pinch points $PP_H = PP_L = 5$. The meanings of different colors is as follows. Red color (label C) is the configuration with greater internal irreversibilities, *i.e.*, with the smaller values of the compressor and expander isentropic efficiencies and with the highest values of pressure drops: $\epsilon_c = \epsilon_t = 0.85$, $\Delta P = 0.03$; Green color (label A) is the configuration with smaller internal irreversibilities, *i.e.*, with the highest values of the compressor and expander isentropic efficiencies and with the smaller values of pressure drops: $\epsilon_c = \epsilon_t = 0.95$, $\Delta P = 0.01$; In between, blue color (label B) denotes the baseline arrangement with intermediate values of parameters: $\epsilon_c = \epsilon_t = 0.9$, $\Delta P = 0.02$. Accordingly, and as expected, note as values of the HE-efficiency, HP coefficient of performance, and round trip efficiency are higher for the most reversible configuration (A, green color), then for the intermediate reversible configuration (B, blue color), and the smaller values correspond to the most irreversible configuration (C, red color).

A complementary view to see the influence of the losses is to focus on the parametric behaviour of magnitudes η, ν, and Φ by the elimination of the r_c^{HP}. This is shown in Fig. 9 for the internal irreversibilities and in Fig. 10 for the external ones. Note here that the different surfaces Φ-η and Φ-ν are clearly separated according to the r_c^{HE}-values. This feature is more visible in the Φ-ν space of the internal losses.

4.4. Pinch points effects

When comparing PP effects (lower panel in Fig. 7 for internal losses and lower panel in Fig. 8 for external losses) the general trend of η, ν, and Φ still remains the same but is it is very clear that the PP requirements play a key role reducing even more the range of acceptable compression ratios r_c^{HE} and r_c^{HP} without appreciable change in the numerical values of the magnitudes. It is noteworthy the strong constraints on the r_c^{HP} values as they rule on the outlet temperature of the working fluid in the HP compressor which should satisfy the PP_H condition in regards to the temperature of the molten salt in the hot tank T_{H1} and in the cold tank T_{H2}. Similar considerations apply to the PP_L

condition in regards to the temperature of the cryogenic liquid in the cold tanks T_{L1} and T_{L2}. This feature is illustrated with more details in the next particular cases.

4.5. Particular configurations

This subsection is intended to show particular configurations with closer approach to check the theoretical predictions for representative molten salts listed in Table 1 and with methanol as cryogenic liquid in all cases.

In the first example, solar salt it is considered in the hot TES and argon as working fluid ($\gamma = 1.667$, $c_{pw} = 0.52$ kJ/kg K) with dimensionless coefficients $\Gamma_H^{HE} = C_w/C_H = 1$, $\Gamma_L^{HE} = C_w/C_L = 0.35$, $\Gamma_H^{HP} = C_w/C_H = 1$, and $\Gamma_L^{HP} = C_w/C_L = 0.35$. The salt temperatures are in the range $511 - 858$ K and the temperatures of the cryogenic liquids in the range $175 - 351$ K. The same standard values are elected for irreversibility parameters (see caption in Table 3).

The results of the model are plotted in Fig. 11 where the HP and HE cycles are depicted in the $T - S$ diagram together with
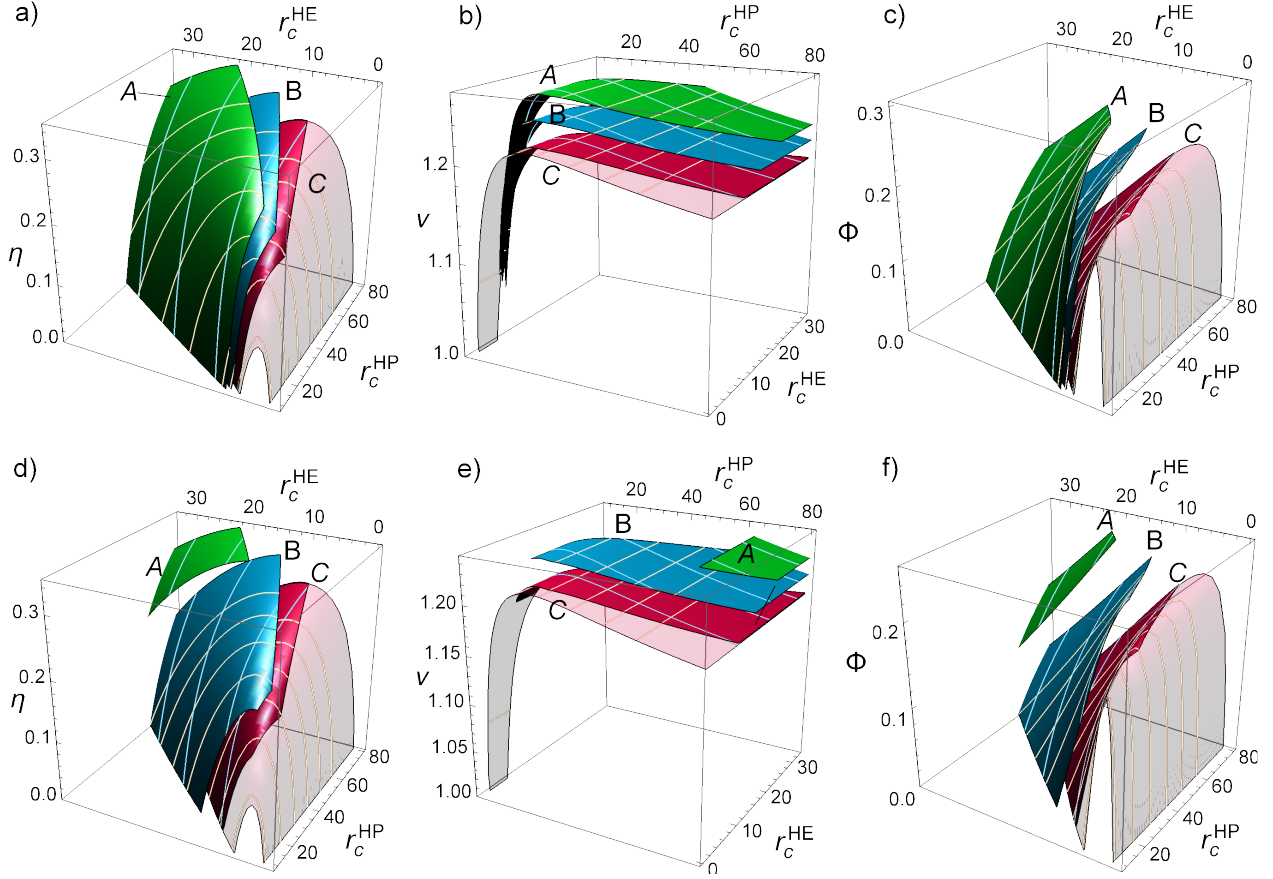
10

Figure 8: In (a)-(c): effects of the external irreversibilities on on the physically acceptable values of η, ν, and Φ versus r_c^{HE} and r_c^{HP} with $PP_H = PP_L = 0$. In (d)-(f) the same but for a pinch points of $PP_H = PP_L = 5$. Red color (label C) $\epsilon_H = \epsilon_L = 0.85$, $\xi = 0.035$ (the configuration with greater external irreversibilities and smaller values of the efficiencies); blue color (label B, baseline arrangement) $\epsilon_H = \epsilon_L = 0.9$, $\xi = 0.020$; and green color (label A) $\epsilon_H = \epsilon_L = 0.95$, $\xi = 0.005$ (the configuration with smaller external irreversibilities and higher values of the efficiencies).
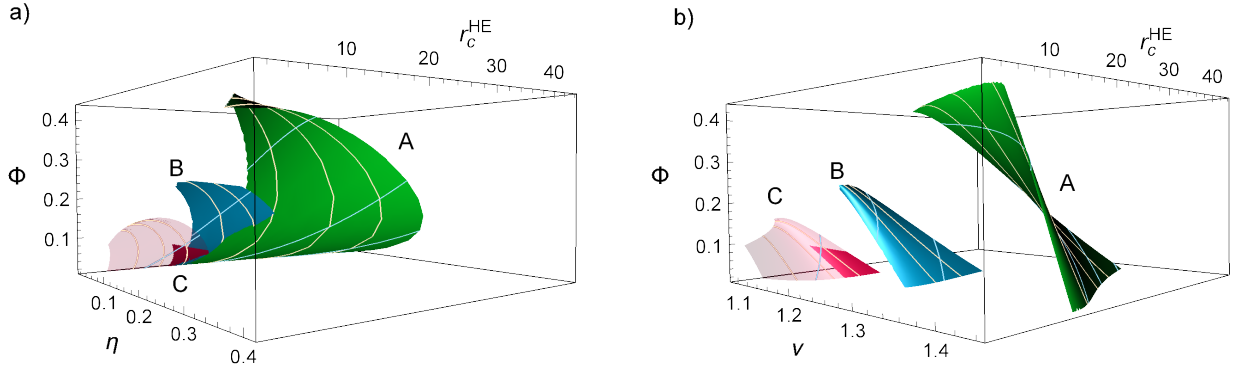

Figure 9: Effects of the internal irreversibilities on the parametric plots of Φ, η and ν versus r_c^{HE} with $PP_H = PP_L = 5$. The legend and numerical values of parameters are the same that in Fig. 7.

the temperature T_{H1}, T_{H2}, T_{L1}, and T_{L2}. These temperatures and those of each state are collected together with the theoretical values of η, ν and Φ in Table 3. Also, it is plotted the physically acceptable parameter space of the r_c^{HE} and r_c^{HP} values according to the input data and characteristics of the solar salt, working fluid, and cryogenic liquid. The red star denote the exact value of r_c^{HE} and r_c^{HP} in the charge and discharge modes for the particular arrangement. Fig. 12 and Table 4 contain the

results for the same system but now the working fluid is air with $\gamma = 1.4$ and $c_{pw} = 1.14$ kJ/kg K. Comparing with results in Fig. 11, it should be stressed the higher compression ratios needed to keep the temperature levels along the cycles, specially in the HP-mode together with the higher S-values (note the different scales of the horizontal axes). Also note that the η, ν, and Φ results are essentially the same.

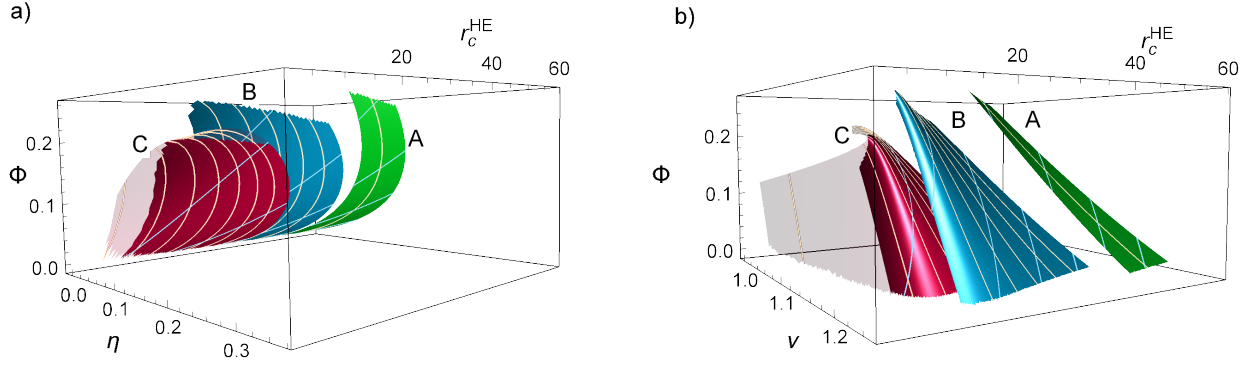Fig. 13 and Table 5 show the results for the carbonate salt

Figure 10: Effects of the external irreversibilities on the parametric plots of Φ, η and ν versus r_c^{HE} with $PP_H = PP_L = 5$. The legend and numerical values of parameters are the same that in Fig. 8.
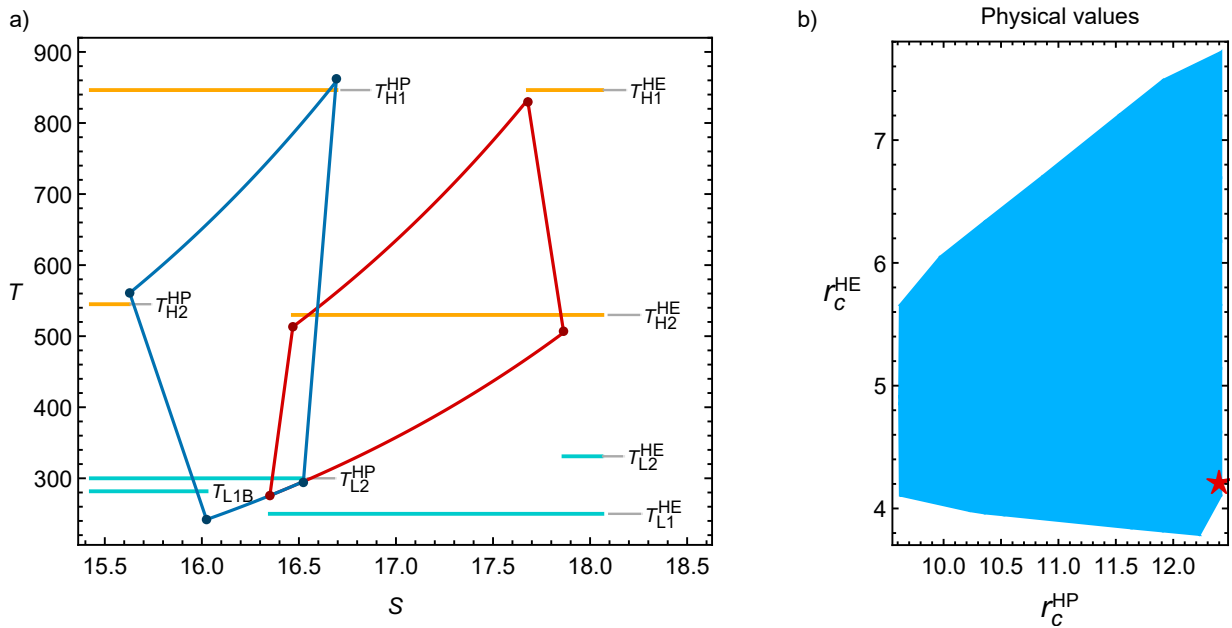

Figure 11: Argon-solar salt-methanol system: T-S cycle (blue is the charge process and red the discharge one) and physically suitable values of the r_c^{HP} and r_c^{HE} values (blue surface); the red star denotes the values of these parameters for the particular depicted configuration. $\epsilon_c = \epsilon_t = 0.9$, $\epsilon_H = 0.95$, $\epsilon_L = 0.9$, $\Delta P = 0.01$, $\xi = 0.02$, $\gamma = 1.667$, $\Gamma_H^{HE} = \Gamma_H^{HP} = 1$, $\Gamma_L^{HE} = \Gamma_L^{HP} = 0.35$, $PP_H = 10\,K$, $PP_L = 4\,K$. Values for the simulation: $T_{max} = 858$ K and $T_{min} = 511$ K are the maximum and minimum values of the salt temperature; $T_{L,max} = 351$ K and $T_{L,min} = 175$ K for the maximum and minimum values of the liquid methanol temperature; and initial value of the $T_{H2}^{HP} = 550\,K$, $r_c^{HP} = 12.4$ and $r_c^{HE} = 4.2$.

in argon ($\gamma = 1.667$, $c_{pw} = 0.52$ kJ/kg K). Note that in this case the minimum and maximum temperatures for the salt are, respectively, 671 K and 1.073 K. As a consequence, compared with the argon-solar salt case, it should be stressed the high level of the hot temperature sources but practically the same range of the entropy values.

Finally, it is noted that the physically suitable values of the compression ratios (blue surfaces in above Figs.) are larger for the HP mode (r_c^{HP}) than for the HE mode (r_c^{HE}), according to comments above in section 4.3. In this way, the outlet temperature of the working fluid in the HP-compressor is enough high to fulfil the PP requirements, especially in the hot side, and the outlet temperature of the working fluid in the HE-compressor is low enough to allow an efficient discharge process.

5. Discussion and Conclusions

Some comments on the accuracy of the obtained results are in order here. As shown on Figs. 6-10, the predicted values of Φ are strongly dependent on the parameters accounting for irreversibilities and, indeed, on the compression ratios. Roughly speaking, the predicted values of Φ are in the range 20-40% depending on the irreversibilities of the different elected configurations. In the considered particular cases, values of Φ are in the range between 34-39%, see Figs. 11-13 and tables 3-5 . It is not easy to make a comparison with other reported values due to the many different theoretical approaches, different cycles, different working fluids, and different media storage used in each case. Values reported by Fernandez *et al.* [11] for transcritical carbon dioxide cycles with and without integration of solar energy amounts
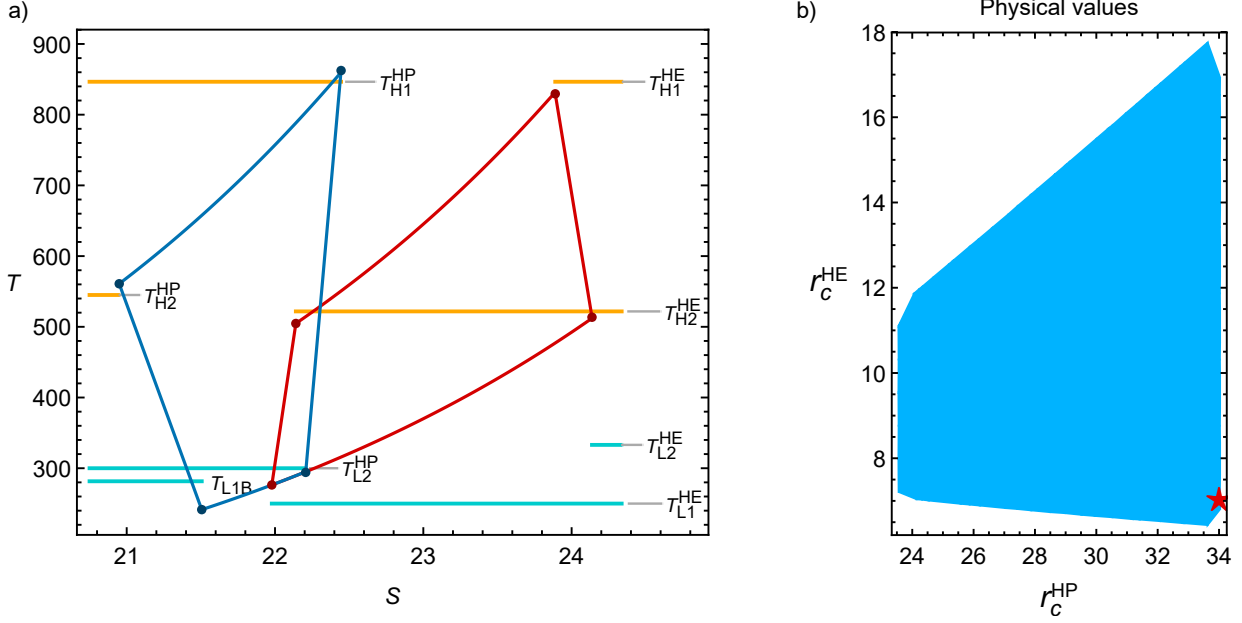
Figure 12: As in Fig. 11 but for the air-solar salt-methanol system. $\epsilon_c = \epsilon_t = 0.9$, $\epsilon_H = 0.95$, $\epsilon_L = 0.9$, $\Delta P = 0.01$, $\xi = 0.02$, $\gamma = 1.4$, $\Gamma_H^{HE} = \Gamma_H^{HP} = 1$, $\Gamma_L^{HE} = \Gamma_L^{HP} = 0.35$, $PP_H = 10\,K$, $PP_L = 4\,K$. Values for the simulation: $T_{max} = 858\,K$ and $T_{min} = 511\,K$ are the maximum and minimum values of the salt temperature; $T_{L,max} = 351\,K$ and $T_{L,min} = 175\,K$ for the maximum and minimum values of the liquid methanol temperature; and initial value of the $T_{H2}^{HP} = 550\,K$, $r_c^{HP} = 34$ and $r_c^{HE} = 7$.
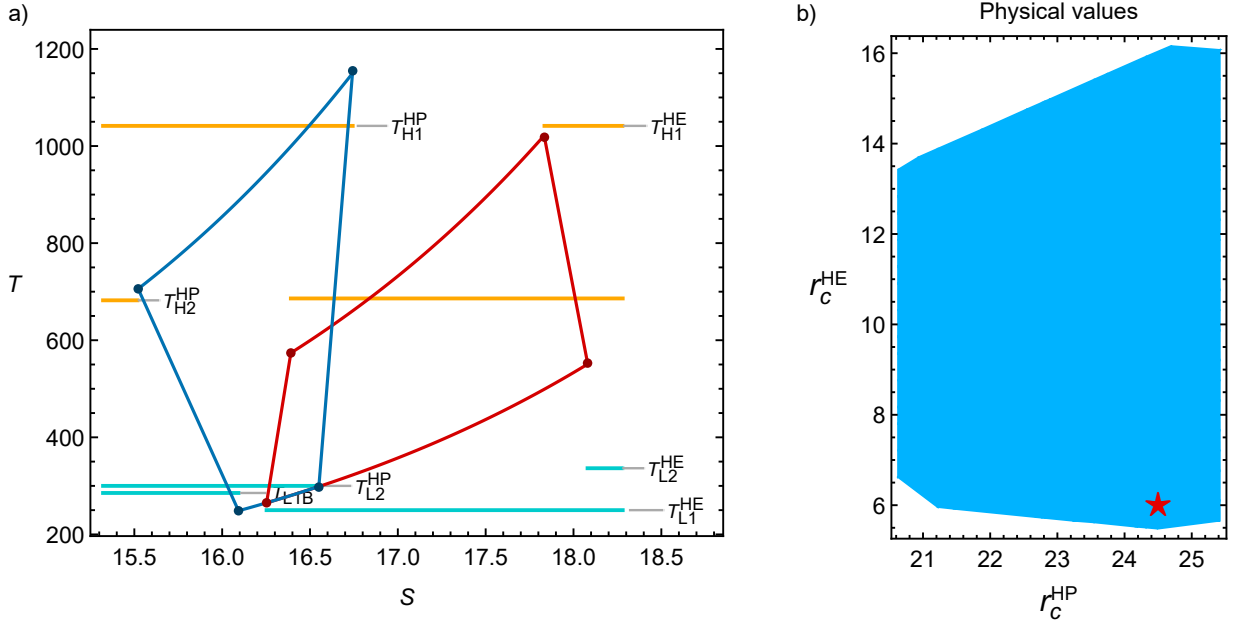

Figure 13: As in Fig. 11 but for the argon-carbonate salt-methanol system. $\epsilon_c = \epsilon_t = 0.9$, $\epsilon_H = \epsilon_L = 0.95$, $\Delta P = 0.01$, $\xi = 0.02$, $\gamma = 1.667$, $\Gamma_H^{HE} = \Gamma_H^{HP} = 0.8$, $\Gamma_L^{HE} = \Gamma_L^{HP} = 0.3$, $PP_H = 10\,K$, $PP_L = 2\,K$. Values for the simulation: $T_{max} = 1070\,K$ and $T_{min} = 671\,K$ are the maximum and minimum values of the salt temperature; $T_{L,max} = 351\,K$ and $T_{L,min} = 175\,K$ for the maximum and minimum values of the liquid methanol temperature; and initial value of the $T_{H2}^{HP} = 690\,K$, $r_c^{HP} = 24.5$ and $r_c^{HE} = 6$.

to 52% and 60%, respectively. Nevertheless, these values could be increased with improved layouts as the one proposed by Morandin *et al.* [18]. Around the same values are those reported ($55 - 60\%$) by Farres *et al.* [19]. Closer to the theoretical predictions in this paper are those given by Benato and Stopatto [5] for a similar cycle but including an additional

electric heater to increase the HP-compression ratio and using different packed bed materials. For example, these authors reported values of Φ around 27% for maximum cycle temperatures of 1000 K, using air as working fluid. Smaller differences for the nine storage materials considered were found. Also, the theoretical predictions by Guo *et al.* [34] are in agreement with

T_{H1}^{HP}	857.5 K	T_{H1}^{HE}	846.3 K		
T_{H2}^{HP}	545 K	T_{H2}^{HE}	529.9 K		
T_{L2}^{HP}	300 K	T_{L2}^{HE}	330.9 K		
T_{L1}^{HP}	281.7 K	T_{L1}^{HE}	250 K	Φ	0.34
T_{1}^{HP}	560.8 K	T_{1}^{HE}	513.2 K	η	0.27
T_{2}^{HP}	862.2 K	T_{2}^{HE}	829.7 K	ν	1.21
T_{3}^{HP}	294.2 K	T_{3}^{HE}	506.9 K		
T_{4}^{HP}	241.9 K	T_{4}^{HE}	275.7 K		

Table 3: Particular configuration argon-solar salt-methanol: temperatures of the hot side (T_{H1}, T_{H2}) and cold side (T_{L1}, T_{L2}) for the charge (HP) and discharge (HE) modes. T_1, T_2, T_3, and T_4 denote the temperatures of the working fluid in the extreme states of the corresponding cycles. η. ν, and Φ are the values of the efficiency, COP, and round trip efficiency, respectively. All values correspond to plot in Fig. 11

T_{H1}^{HP}	857.7 K	T_{H1}^{HE}	846.5 K		
T_{H2}^{HP}	545 K	T_{H2}^{HE}	521.8 K		
T_{L2}^{HP}	300 K	T_{L2}^{HE}	333 K		
T_{L1}^{HP}	281.5 K	T_{L1}^{HE}	250 K	Φ	0.35
T_{1}^{HP}	560.8 K	T_{1}^{HE}	504.7 K	η	0.27
T_{2}^{HP}	862.4 K	T_{2}^{HE}	829.5 K	ν	1.21
T_{3}^{HP}	294.1 K	T_{3}^{HE}	513.6 K		
T_{4}^{HP}	241.5 K	T_{4}^{HE}	276.4 K		

Table 4: As in previous table but for the air-solar salt-methanol. All values correspond to plot in Fig. 12

T_{H1}^{HP}	1056.7 K	T_{H1}^{HE}	1041.5 K		
T_{H2}^{HP}	682.2 K	T_{H2}^{HE}	682.2 K		
T_{L2}^{HP}	300 K	T_{L2}^{HE}	336.3 K		
T_{L1}^{HP}	285.4 K	T_{L1}^{HE}	250 K	Φ	0.39
T_{1}^{HP}	705.8 K	T_{1}^{HE}	573.8 K	η	0.35
T_{2}^{HP}	1155 K	T_{2}^{HE}	1018.1 K	ν	1.12
T_{3}^{HP}	297.4 K	T_{3}^{HE}	552.9 K		
T_{4}^{HP}	248.7 K	T_{4}^{HE}	265.1 K		

Table 5: As in previous table but for the argon-carbonate salt-methanol. All values correspond to plot in Fig. 13

those obtained in this paper. In the same range of values are those reported by Dietrich [17] in an analysis based on Joule cycles for packed bed materials and for heat engine maximum pressure between 2 and 4 bar. However, this author note the great influence on the efficiency values of the inlet and outlet temperatures of the working fluid in the thermal storage media and the pressure drops in the working fluid.

Another key factor regarding the obtained theoretical values

is the assumption made on the thermal properties of solar salts and cryogenic liquids. These properties have been considered as constant for all involved temperature ranges in between T_{min} and T_{max}, as compiled in Tables 1 and 2. Indeed, this a crude assumption in order to keep the steady state thermodynamic model as easy as possible with a reduced set of parameters in order to get an entirely analytical simulation scheme, where it is easy to check the influence of the most important plant design parameters. Then, these values can be considered as average between T_{min} and T_{max}. Obviously, the temperature dependence both of the storage material and of the working fluid should be taken into account, either by appropriate polynomial fits or by using standard reference databases, specially in models focused on storage materials, which is not the case here considered. Calculations reported for air as working fluid with temperature dependent heat capacities in a similar Brayton cycle, gave differences of about 4% in regards with the assumption of diatomic ideal gas with constant heat capacities [43]. The temperature dependence of the density and heat capacity of the liquid materials has not been tested explicitly in this paper. However, it can be inferred that the generic behaviours plotted in all above figures should remain unchanged but concrete numerical values of the calculated magnitudes could change according to the particular molten salt and cryogenic liquid in each case. Two illustrative examples are given by Laughlin in [7], where the temperature dependence of the main thermal properties of the solar salt (including density and heat capacity) are plotted in the interval $500 - 800$ K and those of the n-hexane in all the liquid range (around of $175 - 340$ K). In both cases it can be checked that the variations of C_p and ρ are not very relevant, specially for solar salts. The same constancy for the specific heat of methanol at gas-liquid equilibrium pressure can be checked in [44]. Perhaps, the influence of the temperature of the thermal properties may be more important on the engineering design of the heat exchangers (in order to properly account for the pinch point effects) and when liquid TES media with unbalanced mass flow rates are considered [45].

The present study could be improved along different lines: a) a detailed analysis on the influence of the values of the isentropic efficiencies with different values for the HP and HE cycles. This could introduce subtle behaviors on the charge and discharge modes due to the evident nonlinearity of the coupling; b) the thermodynamic model provides physical insights for design and main losses but a fully optimisation method remains as a complex task where trade-off figures of merit should be tackled by multi-objective and multi-parametric methods in order to obtain the possible Pareto front and the associated space of parameters [46]; c) a third point is the convenience of closed cycles where it may be easier to balance the flow rate of liquid media and the working fluid, avoiding extra losses in the thermal exchanges processes; d) an additional point concerns the possibility of a regenerator (or recuperator). In such a case the coupling of the regenerator and the heat exchangers [47] should be specially fitted in order to keep the storage liquid temperatures but the expected performance improvements must

be faced with a techno-economic analysis [48].

Further improvements should include the specification of time duration of the charge and discharge processes according to grid demands, *i.e.*, a fully dynamical analysis. In this case thermal losses in the surroundings provoke he depletion of stored energy with time. Thus, heat leak should be evaluated as time-dependent processes along the charge, discharge and stabilisation phase. Also the heat transfer processes between the working fluid and liquid media requires finite temperature difference, whose associated losses are linked to the time of the operation mode of the storage liquid. As noted by White *et al.* [14], and at least in packed-bed materials, losses of this kind can vary drastically from a fully discharge/charge process with high temperature gradients to a periodic cycling of the reservoirs with smaller temperature differences but at the expense of reduced storage capacity.

For completeness, costs for the molten salts and of the cryogenic liquids are specified, respectively, in Table 1 and Table 2. Comparison with others storage technologies is presented, for instance, in [7]. The consequent thermo-economic to compute the plant costs and profitability is out of the scope of the present steady-state thermodynamic model.

Acknowledgments

References

[1] A. B. Gallo, J. R. Simoes-Moreira, H. K. Costa, M. M. Santos, and E. Moutinho dos Santos. Energy storage in the energy transition context: A technology review. Renewable and Sustainable Energy Reviews 2016; 65: 800-822.

[2] X. Luo, J. Wang, M. Dooner, and J. Clarke. Overview of current development in electrical energy storage technologies and the application potential in power system operation. Applied Energy 2015; 137: 511-536.

[3] M. C. Argyrou, P. Christodoulides, and S. A. Kalogirou. Energy storage for electricity generation and related processes: Technologies appraisal and grid scale applications. Renewable and Sustainable Energy Reviews 2018: 94: 804-821.

[4] A. Benato and A. Stoppato. Pumped Thermal Electricity Storage: A technology overview. Thermal Science and Engineering Progress 2018; 6: 301-315.

[5] A. Benato and A. Stoppato. Heat transfer fluid and material selection for an innovative Pumped Thermal Electricity Storage system. Energy 2018; 147: 155-168.

[6] R. A. Huggins. Energy Storage Fundamentals, Materials and Applications. Springer, 2016, second edition. ISBN 978-3-319-21239-5

[7] R. B. Laughlin. Pumped thermal grid storage with heat exchange. Journal of Renewable and Sustainable Energy 2017; 9: 1-16.

[8] L. Wan, X. Lin, L. Chai, L. Peng, D. Yu, and H. Chen. Cyclic transient behavior of the Joule-Brayton based pumped heat electricity storage: Modeling and analysis. Renewable and Sustainable Energy Reviews 2019; 111: 523-534.

[9] M. Morandin, F. Maréchal, M. Mercangöt and F. Buchter. Conceptual design of a thermo-electrical energy storage system based on heat integration of thermodynamic cycle: part A Methodology and base case. Energy 2012; 45: 375-385.

[10] M. Morandin, M. Mercangöz, J. Hemrle, F. Maréchal, and D. Favrat. Thermoeconomic design optimization of a thermo-electric energy storage system based on transcritical CO2 cycles. Energy 2013; 58: 571-587.

[11] R. Fernandez, R. Chacartegui, A. Becerra, B. Calderon, and M. Carvalho. Transcritical carbon dioxide charge-discharge energy storage with integration of solar energy. Journal of Sustainable Development of Energy, Water and Environment Systems 2019; 7: 444-465.

[12] T. Desrues, J. Ruer, P. Marty, and J. F. Fourmigué. A thermal energy storage process for large scale electric applications. Applied Thermal Engineering 2010; 30: 425-432.

[13] A. J. White, G. Parks, and C. N. Markides. Thermodynamic analysis of pumped thermal electricity storage. Applied Thermal Engineering 2013; 53: 291-298.

[14] A. White, J. McTigue, and C. Markides. Wave propagation and thermodynamic losses in packed-bed thermal reservoirs for energy storage. Applied Energy 2014; 130: 648-657.

[15] J. D. McTigue, A. J. White, and C. N. Markides. Parametric studies and optimisation of pumped thermal electricity storage. Applied Energy 2015; 137: 800-811.

[16] J. D. McTigue, C. N. Markides, and A. J. White. Performance response of packedbed thermal storage to cycle duration perturbations. Journal of Energy Storage 2018; 19: 379-392.

[17] Axel Dietrich. Assessment of Pumped Heat Electricity Storage Systems through Exergoeconomic Analyses, PhD Thesis, Technishe Universitat Darmstadt, August 2017.

[18] M. Morandin, F. Maréchal, M. Mercangöz, and F. Buchter. Conceptual Design of a Thermo-electrical Energy Storage System Based on Heat Integration of Thermodynamic Cycles: Part B: Alternative System Configurations. Energy 2012; 45: 386-396.

[19] P. Farres-Antunez, J. D. McTigue, A. J. White. A pumped thermal energy storage cycle with capacity for concentrated solar power integration. March Offshore Energy and Storage Summit (OSES). 2019 Brest, France; DOI: 10.1109/OSES.2019.8867222.

[20] G. Francesco Frate, L. Ferrari, U. Desideri. Multi-criteria investigation of a pumped thermal electricity storage (PTES) system with thermal integration and sensible heat storage. Energy Conversion and Management 2020; 208: 112530.

[21] A. H. Hassan, L. O'Donoghue, V. Sánchez-Canales, J. M. Corberán, J. Payá, H. Jockenhöfer. Thermodynamic analysis of high-temperature pumped thermal energy storage systems: Refrigerant selection, performance and limitations. Energy Reports. In press. https://doi.org/10.1016/j.egyr.2020.05.010

[22] F. Zaversky, J. García-Barberena, M. Sánchez, and D. Astrain. Transient molten salt two-tank thermal storage modeling for CSP performance simulations. Solar Energy 2013; 93: 294-311.

[23] N. Peger, T. Bauer, C. Martin, M. Eck, and A. Wörner. Thermal energy storage: overview and specific insight into nitrate salts for sensible and latent heat storage. Journal of Nanotechnology 2015; 6: 1487-1497.

[24] C. S. Turchi, J. Vidal, and M. Bauer. Molten salt power towers operating at 600-650: Salt selection and cost benefits. Solar Energy 2018: 164: 38-46.

[25] Y. Cengel, Heat Transfer. A practical approach. McGraw-Hill Education, second edition, 2002. ISBN-10: 9780072458930

[26] T. R. Davenne, S. D. Garvey, B. Cardenas, and M. C. Simpson. The cold store for a pumped thermal energy storage system. Journal of Energy Storage 2017;14: 295-310.

[27] J. M. P. Tournier and M. S. El-Genk. Properties of noble gases and binary mixtures for closed Brayton Cycle applications. Energy Conversion and Management 2008; 49: 469-492.

[28] H. Habibi, M. Zoghi, A. Chitsaz, K. Javaherdeh, M. Ayazpour, and E. Bellos. Working fuid selection for regenerative supercritical Brayton cycle combined with bottoming ORC driven by molten salt solar power tower using energy and exergy analysis. Sustainable Energy Technologies and Assessments 2020; 39: article 100699.

[29] Z. Wan, J. Wei, M. A. Qaisrani, J. Fang, and N. Tu. Evaluation on thermal and mechanical performance of the hot tank in the two-tank molten salt heat storage system. Applied Thermal Engineering 2020; 167: article114775.

[30] A. Thess. Thermodynamic efficiency of pumped heat electricity storage. Physical Review Letters 2013; 111: article 110602.

[31] J. Chen and J. Guo, Comment on Thermodynamic efficiency of pumped heat electricity storage. Physical Review Letters 2016; 116: article 158901.

[32] J. Guo, H. Yang, and B. Lin. Performance characteristics and parametric optimization of weak dissipative pumped thermal electricity storage system. Energy Conversion and Management 2018; 157: 527-535.

[33] J. Guo, L. Cai, J. Chen, and Y. Zhou. Performance optimization and comparison of pumped thermal and pumped cryogenic electricity storage system. Energy 2016; 106: 260-269.

[34] J. Guo, L. Cai, J. Chen, and Y. Zhou. Performance evaluation and parametric choice criteria of a Brayton pumped thermal electricity storage system. Energy 2016; 113: 693-701.

[35] https://tradingeconomics.com/commodity/propane

[36] J. M. M. Roco, S. Velasco, A. Medina, and A. C. Hernandez. Optimum performance of a regenerative Brayton thermal cycle. Journal of Applied Physics 2001; 82: 2735-2741.

[37] A. J. White. Thermodynamic analysis of the reversed Joule-Brayton cycle heat pump for domestic heating. Applied Energy 2009; 86: 2243-2450.

[38] M. H. Ahmadi, M. A. Ahmadi, F. Pourfayaz, M. Bidi. Thermodynamic analysis and optimization for an irreversible heat pump working on reversed Brayton cycle. Energy Conversion and Management 2016; 110: 260-267.

[39] A. Bejan. Advanced Engineering Thermodynamics. Wiley, New York, 1988, Chap. 8.

[40] A. K. Araujo and G. I. Medina. Analysis of the effects of climatic conditions, loading level and operating temperature on the heat losses of two-tank thermal storage systems in CSP. Solar Energy 2018; 176: 358-369.

[41] N. Mahdavi and S. Khalilarya. A novel method for assessment of pinch point characteristics of heat exchangers with different combinations of pure fluid and binary mixture as hot and cold streams. Energy Conversion and Management 2019; 181: 342-358.

[42] S. Sánchez-Orgaz, A. Medina, A. Calvo Hernández. Thermodynamic model and optimization of a multi-step irreversible Brayton cycle. Energy Conversion and Management 2010; 51: 2134-2143.

[43] R. P. Merchán, M. J. Santos, A. Medina, A. Calvo Hernández Thermodynamic model of a hybrid Brayton thermosolar plant. Renewable Energy 2018; 128: 473-483.

[44] https://www.engineeringtoolbox.com/methanol

[45] L. Wan, X. Lin, L. Chai, L. Peng, D. Yu, J. Liu, and H. Chen. Unbalanced mass flow rate of packed bet thermal energy storage and its influence on the Joule-Brayton based pumped thermal electricity storage. Energy Conversion and Management 2019; 185: 593-602.

[46] S. Sánchez-Orgaz, M. Pedemonte, P. Ezzatti, P. L. Curto-Risso, A. Calvo Hernández. Multi-objective optimization of a multi-step solar-driven Brayton plant. Energy Conversion and Management 2015; 99: 346-358.

[47] S. Sánchez-Orgaz, A. Medina, A. Calvo Hernández. Recuperative solar-driven multi-step gas turbine power plants. Energy Conversion and Management 2013; 67: 171-178.

[48] M. Mahdi Naserian, S. Farahat, F. Sarhaddi. Exergoeconomic multi objective optimization and sensitivity analysis of a regenerative Brayton cycle. Energy Conversion and Management 2016; 117: 95-105.